



Safe Motion Control of Autonomous Vehicle Ski-Stunt Maneuvers

Feng Han D, Graduate Student Member, IEEE, and Jingang Yi D, Senior Member, IEEE

Abstract—A ski-stunt maneuver is a type of aggressive vehicle motions in which a four-wheel vehicle runs on two wheels on one side, and the other two wheels are lifted in the air. It is a challenging task even for skilled car drivers to perform a ski-stunt maneuver. We present the safety-guaranteed motion control of autonomous ski-stunt maneuvers. Inspired by bicycle dynamics, a vehicle dynamic model is first built for ski-stunt motion. To prevent possible rollovers, a control barrier function is used in a model predictive control formulation to plan a safe motion trajectory. A motion controller is then designed to follow the safe trajectory with guaranteed balance. Ski-stunt maneuver initiation and switching strategies are also analyzed and designed. Extensive experiments are conducted using a scaled truck platform to demonstrate the control design. The experimental results confirm that the vehicle can successfully initiate the ski-stunt maneuver to safely navigate among obstacles and narrow passes and then switch back to normal driving.

Index Terms—Aggressive maneuvers, control barrier function (CBF), ski-stunt maneuver, vehicle dynamics and control.

I. INTRODUCTION

SKI-STUNT maneuver is an aggressive vehicle motion in which a four-wheel vehicle moves on only two wheels on one side, with the other two wheels lifted in the air. Similar to other aggressive driving skills [1], [2], [3], the ski-stunt maneuver is usually performed by professional drivers. To initiate a ski-stunt maneuver, one can drive the vehicle on a ramp to lift one side and continue maintaining the balance of the tilted vehicle body by controlling the steering and velocity. For vehicles with a high center of gravity (e.g., sport utility vehicles and trucks), a ski-stunt maneuver can also be initiated by rapidly changing steering angle, but this strategy would likely lead to rollover incident [4].

Manuscript received 13 February 2023; revised 22 June 2023; accepted 24 November 2023. Date of publication 20 December 2023; date of current version 16 August 2024. Recommended by Technical Editor Q. Ahmed and Senior Editor M. Indri. This work was supported in part by the US National Science Foundation Under Grant CNS-1932370. (Corresponding author: Jingang Yi.)

The authors are with the Department of Mechanical and Aerospace Engineering, Rutgers University, Piscataway, NJ 08854 USA (e-mail: fh233@scarletmail.rutgers.edu; jgyi@rutgers.edu).

This article has supplementary material provided by the authors and color versions of one or more figures available at https://doi.org/10.1109/TMECH.2023.3338016.

Digital Object Identifier 10.1109/TMECH.2023.3338016

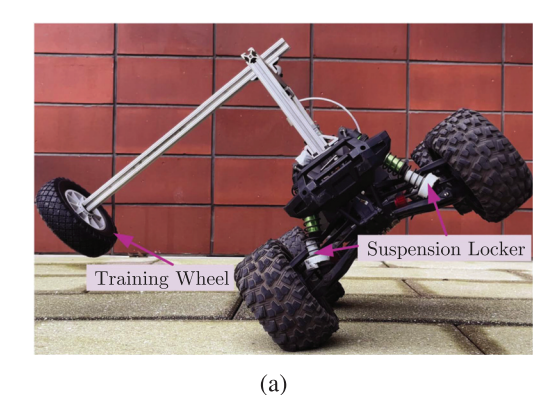
Autonomous ski-stunt maneuvers can potentially be used as an active safety feature for obstacle avoidance, narrow-road passage, and other emergency procedures [4], [5]. A vehicle undergoing a ski-stunt maneuver experiences a large roll angle in a highly controlled fashion [6], [7]. Vehicle motion in a ski-stunt maneuver must be under safe control with rollover prevention guaranteed. Extensive research has been reported for vehicle rollover prevention [6], [8], [9]. Restriction of a large roll angle is the main goal of motion control in these designs. In contrast, when running on two wheels on one side, the vehicle displays single-track motion that is similar to bicycles. The motion and balance control of autonomous bicycles have been successfully developed under steering and velocity actuation (e.g., [10], [11], [12], [13], [14]). However, unlike bicycle dynamics, large tire camber angle in ski-stunt maneuver results in limited actuation and brings additional challenges for motion control design.

Without using ramps, it is challenging to initiate a ski-stunt maneuver and maintain balance only by steering actuation. In particular, a safety-guaranteed motion control design is needed for vehicle rollover prevention. The control barrier function (CBF) method is one approach to incorporate safety-critical requirements. In robot and vehicle control applications (e.g., [15], [16], [17]), CBF has been used as a dynamic constraint to filter the nominal control for a safety-guaranteed design. For motion control of ski-stunt maneuver, the CBF-based method has to deal with underactuated, nonminimum-phase vehicle dynamics, i.e., the vehicle motion has three degrees of freedom (DOFs) but with only steering and velocity actuation as two control inputs. In [10], an external and internal convertible (EIC) control method was presented for underactuated balance robots. We extend the EIC control design to incorporate CBFs.

We present a safety-guaranteed motion control for autonomous ski-stunt maneuvers. Kinematic and dynamic models are used for four- and two-wheel planar motion in ski-stunt maneuvers. To cope with the underactuated robot dynamics and balance requirements, we formulate a model predictive control (MPC)-based trajectory planning design, with consideration of CBF constraints for rollover prevention and collision avoidance. The balance control is guaranteed by stabilizing the roll motion on balance equilibrium manifold [10], [18]. Under the proposed control, closed-loop stability and motion safety are analyzed and guaranteed. We demonstrate motion control performance with extensive experiments using a scaled truck testbed.

The main contribution of this work is the novel safety-andbalance-guaranteed control for ski-stunt maneuvers. To our best knowledge, there has been no reported work on autonomous

1083-4435 © 2023 IEEE. Personal use is permitted, but republication/redistribution requires IEEE permission. See https://www.ieee.org/publications/rights/index.html for more information.



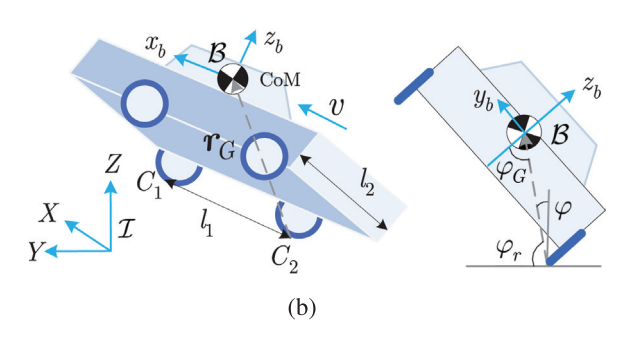


Fig. 1. (a) Ski-stunt maneuver. (b) Side- and back- views of the kinematics of vehicle motion in a ski-stunt maneuver.

vehicle ski-stunt maneuvers and this is the first study to successfully demonstrate the safety-guaranteed control for the highly agile motion. Compared to the previous conference presentation [19], we demonstrate a motion control design with guaranteed safety. The closed-loop stability and motion control switching strategies are new. Finally, mechatronic design and extensive experiments are demonstrated in this work. The proposed control method can further be extended to other underactuated robots and vehicles [14], [20], [21]. The main purpose of this work is to demonstrate the feasibility of autonomous ski-stunt maneuvers by a motion control design and application to a scaled vehicle. Further developments still remain to be implemented on a full-size vehicle.

The rest of this article is organized as follows. In Section II, we present the vehicle dynamics model for ski-stunt maneuvers. The safe trajectory planning and control are presented in Section III. We discuss motion control switching strategies in Section IV. The experiments are presented in Section V. Finally, Section VI concludes this article.

II. VEHICLE DYNAMICS MODELS

A. System Configuration and Problem Statement

Fig. 1(a) shows a snapshot of the experimental platform performing a ski-stunt maneuver. Fig. 1(b) illustrates the kinematics of the vehicle from side and back views. We denote the frontand rear-wheel ground contact points as C_1 and C_2 , respectively. Two coordinate frames are set up: 1) the inertial frame \mathcal{I} that is fixed on the ground with the Z-axis upward; and 2) the body frame \mathcal{B} that is fixed at the center of mass (CoM) of the vehicle

with the z_b -axis upward. The vehicle is assumed to move only on a flat ground surface.

The planar motion of the vehicle is captured by point C_2 and its position is denoted as $r=[x\ y]^T$ in $\mathcal I$. The vehicle's wheelbase and width are denoted as $l_1=\overline{C_1C_2}$ and l_2 , respectively. The distances between the CoM and C_2 along the x_b -, y_b -, and z_b -axis directions in $\mathcal B$ are denoted as x_G,y_G , and z_G , respectively. The vehicle's yaw, roll, and steering angles are denoted as ψ,φ , and ψ , respectively. The zero roll angle $\psi=0$ is defined at the static equilibrium point, i.e., the CoM projection point on the ground is located on the C_1C_2 line. It is clear from Fig. 1(b) that the position of $\psi=0$ corresponds to rotating the vehicle by angle $\psi=0$ along the $\psi=0$ along the $\psi=0$ and it is straightforward to obtain that $\psi=0$ at four-wheel driving condition.

Vehicle velocity and steering angle are the two control actuations, while the vehicle has three DOFs (i.e., r and φ) during ski-stunt motion. We consider the following motion control problem.

Problem Statement: For a given desired trajectory r_d , the goal of motion controller is to initiate and maintain a ski-stunt maneuver from a four-wheel driving condition by velocity and steering actuation such that r follows r_d closely, while the roll motion is kept balanced when vehicle running on two wheels.

B. Vehicle Motion Models

The vehicle is assumed to operate on high-friction ground such that the contact point C_2 has zero lateral velocity, i.e., non-holonomic constraint at C_2 . To simplify the modeling method, we take a kinematic model for the planar motion and a dynamic model for the roll motion. We denote the longitudinal velocity of point C_2 as v, and the vehicle kinematic model is written as $\dot{x} = v \cos \psi$ and $\dot{y} = v \sin \psi$. Taking the derivative of \dot{r} , we obtain

$$\ddot{\boldsymbol{r}} = \begin{bmatrix} \ddot{x} \\ \ddot{y} \end{bmatrix} = \underbrace{\begin{bmatrix} \cos \psi & -v \sin \psi \\ \sin \psi & v \cos \psi \end{bmatrix}}_{\boldsymbol{g}_r} \begin{bmatrix} \dot{v} \\ \dot{\psi} \end{bmatrix} = \boldsymbol{g}_r \boldsymbol{u}$$
(1)

where control input $u = [u_v \ u_{\psi}]^T$, $u_v = \dot{v}$ and $u_{\psi} = \dot{\psi}$. The relationship between steering and yaw motion is given as [14]

$$\dot{\psi} = \frac{v}{l_1 \cos \varphi_r} \tan \phi. \tag{2}$$

The kinematic model (1) is used for both four- and two-wheel planar motion control of the vehicle.

During a ski-stunt maneuver, the roll motion is modeled as an inverted pendulum and a dynamics model is obtained. The total vehicle mass and mass moments of inertia about the CoM along the x_b , y_b , and z_b -axis directions are denoted as m and J_x , J_y , and J_z , respectively. Similar to the bicycle dynamics in [14], using the Lagrangian method, we obtain the equation of motion for roll motion as

$$J_t \ddot{\varphi} - mgl_G \sin \varphi = ml_G x_G \ddot{\psi} \cos \psi + ml_G^2 \dot{\psi}^2 \sin \varphi \cos \varphi$$
$$+ \left(J_z \cos^2 \varphi + J_y \sin^2 \varphi \right) \dot{\psi}^2 - \left(ml_G x_G \dot{\varphi} \sin \varphi \right)$$

$$-vl_G m\cos\varphi)\dot{\psi}\tag{3}$$

where $J_t = ml_G^2 + J_x$ and $l_G = \sqrt{y_G^2 + z_G^2}$. Noting that $v \gg |\dot{\psi}|, |\dot{\varphi}|$, we simplify (3) by neglecting the higher-order terms and obtain

$$\ddot{\varphi} = f_{\varphi} + g_{\varphi} u_{\psi} + f_{u} \tag{4}$$

where $f_{\varphi} = \frac{1}{J_t} mgl_G \sin \varphi$, $g_{\varphi} = \frac{1}{J_t} mvl_G \cos \varphi$, and f_u is a bounded term to account for the torque approximation errors and uncertainties.

Letting $x = [r^T \ \varphi \ \dot{r}^T \ \dot{\varphi}]^T \in \mathbb{R}^6$, the system models (1) and (4) are rewritten as

$$\dot{x} = F + Gu + F_{u} \tag{5}$$

where $\boldsymbol{F} = [\mathbf{0}_{1\times 5} \ f_{\varphi}]^T$, $\boldsymbol{F}_u = [\mathbf{0}_{1\times 5} \ f_u]^T$, $\boldsymbol{G} = [\mathbf{0}_{2\times 3} \ \boldsymbol{g}_r^T]^T$, $\boldsymbol{g}_{\varphi} = [0 \ g_{\varphi}]$, and $\mathbf{0}_{p\times q}$ represents zero matrix with dimension $p\times q, p, q\in\mathbb{N}$.

III. MOTION CONTROL OF SKI-STUNT MANEUVER

In this section, we first introduce the exponential CBF (ECBF), and then present the safe motion control and analysis for ski-stunt maneuvers.

A. Safety Criteria and ECBF

The following safety criteria are considered.

- 1) Rollover prevention: When conducting ski-stunt maneuvers, any rollovers should be prevented, i.e., $\varphi < \varphi_{\max}$, where φ_{\max} is the allowable maximum roll angle.
- 2) *Roll balance:* The vehicle should be dynamically balanced around equilibrium points when navigating on two wheels.
- 3) *Collision avoidance*: Any possible collision with obstacles (if present) should be avoided.

Safety and balance are two major control objectives. Since roll and planar motions are tightly coupled, rollovers may happen due to either sharply turning at high speed or following unsafe roll-angle profiles. The safety set is defined by CBF $h(\boldsymbol{x})$ as

$$S = \{x : h(x) \ge 0\}. \tag{6}$$

Function h(x) is assumed to have the relative degree $p \in \mathbb{N}$, i.e., the control input u appears in the pth derivative of h(x) explicitly. To define the ECBF for (5), we introduce $q = [h(x) \ h'(x) \ \cdots \ h^{(p-1)}(x)]^T \in \mathbb{R}^p$ and obtain

$$\dot{q} = Aq + Bu_h + u_\delta \tag{7}$$

and output $h(\boldsymbol{x}) = \boldsymbol{C}\boldsymbol{q}$ with $\boldsymbol{C} = [1 \ \boldsymbol{0}_{v-1}^T]$

$$m{A} = egin{bmatrix} 0 & m{I}_{p-1} \ 0 & 0 \end{bmatrix}, m{B} = egin{bmatrix} m{0}_{p-1} \ 1 \end{bmatrix}, m{u}_{\delta} = egin{bmatrix} m{0}_{p-1} \ rac{\partial m{h}}{\partial m{x}} m{F}_{u} \end{bmatrix},$$

 I_{p-1} and $\mathbf{0}_{p-1}$ are the identity matrix and zero (column) vector with dimension p-1, respectively, $u_h = L_F^p h(\boldsymbol{x}) + L_G L_F^{p-1} h(\boldsymbol{x}) \boldsymbol{u}$, $L_F^p h(\boldsymbol{x})$ is the pth order Lie derivative of $h(\boldsymbol{x})$ along vector field \boldsymbol{F} , and $L_G L_F^{p-1} h(\boldsymbol{x})$ is assumed to be invertible.

We take a state feedback control $u_h = -\gamma q$, $\gamma^T \in \mathbb{R}^p$, such that under u_h the system (7) with $u_{\delta} = 0$ is asymptotically stable. The closed-loop solution is then obtained as

$$h(\boldsymbol{x}) = \underbrace{\boldsymbol{C}e^{-(\boldsymbol{A}-\boldsymbol{B}\boldsymbol{\gamma})t}\boldsymbol{q}(0)}_{h_u(\boldsymbol{x})} + \underbrace{\int_0^t \boldsymbol{C}e^{-(\boldsymbol{A}-\boldsymbol{B}\boldsymbol{\gamma})\tau}\boldsymbol{u}_\delta(t-\tau)d\tau}_{h_\delta(\boldsymbol{x})}$$

$$= h_u(\boldsymbol{x}) + h_\delta(\boldsymbol{x}). \tag{8}$$

If the system model is precise, namely $h_{\delta}(x)=0$, h(x) is referred as the ECBF. When $u_h>-\gamma q$, $h_u(x)\geq Ce^{(A-B\gamma)t}$ q(0) for t>0. If $h_u(x)>0$ at t=0, the system remains safe for $h_u>0$ [15], [22]. Given bounded F_u , we obtain that $h_{\delta}(x)$ is bounded $|h_{\delta}|\leq h_{\delta}^{\max}$ for t>0 and $h(x)\geq -h_{\delta}^{\max}$. Compared with the conventional CBF, h(x) in (8) might reach a negative value due to model accuracy. To avoid this, we estimate the value of h_{δ}^{\max} and add a safety buffer as a conservative measure.

The control input set for $x \in \mathcal{S}$ is defined as

$$\mathcal{U}_s = \{ \boldsymbol{u} \in \mathcal{U} : L_F^p h(\boldsymbol{x}) + L_G L_F^{p-1} h(\boldsymbol{x}) \boldsymbol{u} \ge -\gamma \boldsymbol{q}(\boldsymbol{x}) \}. \tag{9}$$

Safe control can be obtained through a safety-critical design [15]. The safety-critical control does not explicitly design the control input. Instead, the CBF is employed as a constraint to modify the nominal control [23].

B. Safe Ski-Stunt Maneuver Planning and Control

We first use the CBF method as an online motion planner to obtain a safe trajectory and then design a controller to follow the planned safe trajectory. The approach is summarized into the following steps: 1) conduct the nominal control design; 2) modify nominal control and plan the safe trajectory; and 3) calculate roll balance equilibrium manifold (BEM) and design the controller to follow the safety trajectory and the BEM. The CBF is integrated with the motion planning and vehicle dynamics are considered in the last step of feedback controller design.

The nominal control u_n is designed such that the planar motion converges to r_d . Using the kinematic model (1), we design the nominal control

$$\boldsymbol{u}_n = \boldsymbol{g}_r^{-1}(v, \psi)\boldsymbol{u}_{nr}, \ \boldsymbol{u}_{nr} = \ddot{\boldsymbol{r}}_d - k_{p1}\boldsymbol{e}_r - k_{d1}\dot{\boldsymbol{e}}_r$$
(10)

where $e_r = r - r_d$ and $k_{p1}, k_{d1} > 0$ are constant gains. We design the roll motion CBF $h_{\omega}(x)$ as

$$h_{\varphi}(\boldsymbol{x}) = \varphi_1^2 - (\varphi - \varphi_2)^2 \tag{11}$$

where φ_1 and φ_2 are constant. When $h_{\varphi}(x) > 0$, the roll angle is confined in a tube around φ_2 with the radius of φ_1 to prevent a rollover. The allowable maximum roll angle is $\varphi_{\max} = \varphi_1 + \varphi_2$. For collision avoidance, the following CBF is used to evaluate the distance to an obstacle at (x_o, y_o) :

$$h_r(\mathbf{x}) = R^2 - (x - x_o)^2 - (y - y_o)^2$$
 (12)

where R is the allowed safety distance.

To obtain a safe trajectory, we formulate an MPC-based online planner as

$$\min_{\boldsymbol{u}_H} \int_t^{t+H\Delta t} \left(\boldsymbol{e}_{sd}^T \boldsymbol{W}_1 \boldsymbol{e}_{sd} + \boldsymbol{e}_u^T \boldsymbol{W}_2 \boldsymbol{e}_u \right) d\tau \quad (13a)$$

subject to:
$$\dot{x}_s = F + Gu_s$$
 (13b)

$$L_F^p h_r(\boldsymbol{x}_s) + L_G L_F^{p-1} h_r(\boldsymbol{x}_s) \boldsymbol{u}_s \ge -\gamma_r \boldsymbol{q}(\boldsymbol{x}_s), \quad (13c)$$

$$L_F^p h_{\varphi}(\boldsymbol{x}_s) + L_G L_F^{p-1} h_{\varphi}(\boldsymbol{x}_s) \boldsymbol{u}_s \ge -\gamma_{\varphi} \boldsymbol{q}(\boldsymbol{x}_s)$$
 (13d)

where $u_H = \{u_{s1}, \dots, u_{sH}\}$ is the predictive control input set, Δt is the step length, $H \in \mathbb{N}$ is the predictive horizon, and W_1, W_2 are positive definite diagonal matrices. Term $e_u = u_s - u_n$, $u_s \in \mathcal{U}_s$, is the input difference between u_s and normal control u_n . Error $e_{sd} = x_s - x_d$ is the difference between the safe trajectory x_s and the desired trajectory x_d . The desired roll angle φ_e and its derivative $\dot{\varphi}_e$ of x_d are approximated by the BEM that will be given later in this section. The optimization in (13) is solved online in real time via sequential quadratic programming. The nominal control is used as the initial guess.

Under the solution u_s^* of (13), the predicted safe trajectory is r_s , which is computed by (13b). With safe trajectory r_s , the control input is obtained similar to (10) as

$$\boldsymbol{u}_{sn} = [u_{sv} \ u_{s\psi}]^T = \boldsymbol{g}_r^{-1}(v, \psi)\boldsymbol{u}_r, \ \boldsymbol{u}_r = \ddot{\boldsymbol{r}}_s - k_{p1}\boldsymbol{e}_s - k_{d1}\dot{\boldsymbol{e}}_s$$
(14)

where $e_s = r - r_s$. To guarantee balance of roll motion, we first compute the BEM and then update the steering control input for roll motion stabilization. Given $u_{s\psi}$ in (14), the BEM is defined as the instantaneous roll angle equilibrium, i.e.,

$$\mathcal{E} = \{ \varphi_e : f_{\varphi}(\varphi_e) + g_{\varphi}(\varphi_e) u_{s\psi} = 0 \}. \tag{15}$$

To stabilize φ onto \mathcal{E} , we update the steering control input

$$u_{\varphi\psi} = g_{\varphi}^{-1}(-f_{\varphi} + \ddot{\varphi}_{e} - k_{p2}e_{\varphi} - k_{d2}\dot{e}_{\varphi})$$
 (16)

where $e_{\varphi} = \varphi - \varphi_e$ and $k_{p2}, k_{d2} > 0$ are feedback gains. The final control becomes $u_f = [u_{sv} \ u_{\varphi\psi}]$.

Algorithm 1 illustrates the overall motion control for the skistunt maneuver. In the algorithm, lines 2 to 7 are interpreted as an online CBF-based trajectory planning, where a family of safety-involved CBFs are considered as dynamic constraints for both the planar and roll motion. Finally, lines 8 to 10 represent the control design for the autonomous ski-stunt maneuver.

Defining error vector $e_x = [e_s^T \ e_{\varphi} \ \dot{e}_s^T \ \dot{e}_{\varphi}]^T$, we assume that the model perturbation error of the closed-loop system by using the BEM (15) is affine with e_x . The stability and convergence of the control design are then summarized in the following lemma with proof given in Appendix.

Lemma 1: For (5) under the controller u_f , safe criteria $x \in \mathcal{S}$, balance condition $\varphi \in \mathcal{E}$, and exponentially trajectory tracking to a neighborhood of r_d are simultaneously achieved.

IV. MOTION CONTROL SWITCHING STRATEGY

In this section, we discuss how to switch motions between regular four-wheel driving and ski-stunt maneuver. The initiation of a ski-stunt maneuver is challenging, and the highest priority should be given to rollover prevention. To systematically

Algorithm 1: Safe Control Design for Ski-Stunt Maneuver.

```
1 Specify W_1, W_2, \gamma_i, \epsilon, k_{pj}, k_{dj}, H, \Delta t, and t_F;
 2 Design the CBF functions h_r(\mathbf{x}) and h_{\varphi}(\mathbf{x}), t=0;
 3 while t < t_F do
        Design the nominal control u_n by (10);
 5
        Safe control design: Solve (13) to obtain u_s^*;
        Safe reference update: Obtain r_s by (13b) using
         u^*:
        Planar motion control: Design control u_s by (14);
 8
        Calculate BEM: Obtain the BEM by (15);
        Roll motion control: Update steering control
         u_{\psi\varphi} (16) for balance control;
        Actual control: Calculate u_f = [u_{sv} \ u_{\varphi\psi}]^T for
         steering and velocity actuation;
11
        t = t + \Delta t;
```

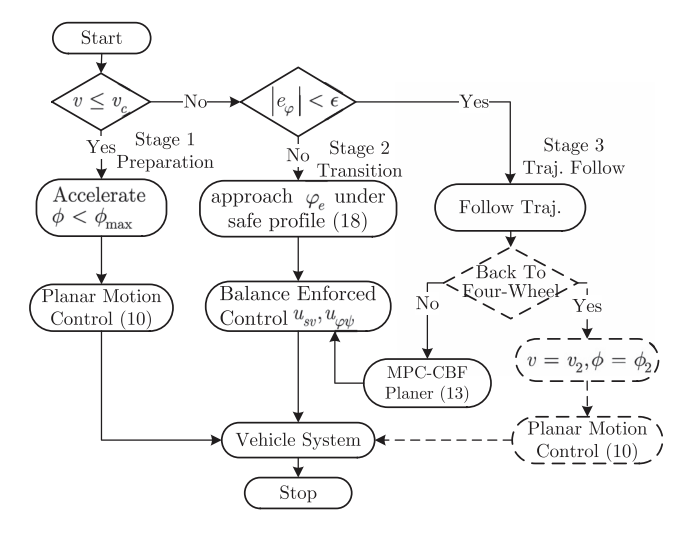


Fig. 2. Schematic of the design flowchart for initiation of the ski-stunt maneuver, and motion-control switching strategies. The blocks with dashed lines indicate the four-wheel driving condition.

design an initiation strategy, we consider a three-stage process: 1) maneuver preparation; 2) motion transition from on four- to two-wheel modes; and 3) fully ski-stunt maneuvering. Fig. 2 illustrates the flowchart of the three-stage process as well as the corresponding control strategies.

1) Stage 1: This stage serves as a preparation phase. A sharp turn (i.e., a large steering angle change) is required to generate the turning torque, while at the same time, the steering angle should be kept within a limit, i.e., $\phi < \phi_{\rm max}$, where $\phi_{\rm max}$ denotes the maximum allowable steering angle.

To help generate enough torque for initiation, the vehicle velocity should increase to reach a threshold value, v_c . The steering-induced torque $\tau_s = mvl_G\cos\varphi u_\psi = \frac{mv^2l_G\cos\varphi}{l_1\cos\varphi_r}\tan\phi$ is proportional to vehicle velocity square. When the vehicle starts to tilt its body, $\varphi_r = 0$ (or $\varphi = -\varphi_G$), the steering-induced turning torque τ_s is equal to the gravitational torque (i.e., $mgl_G\sin\varphi$). From this observation, we obtain the

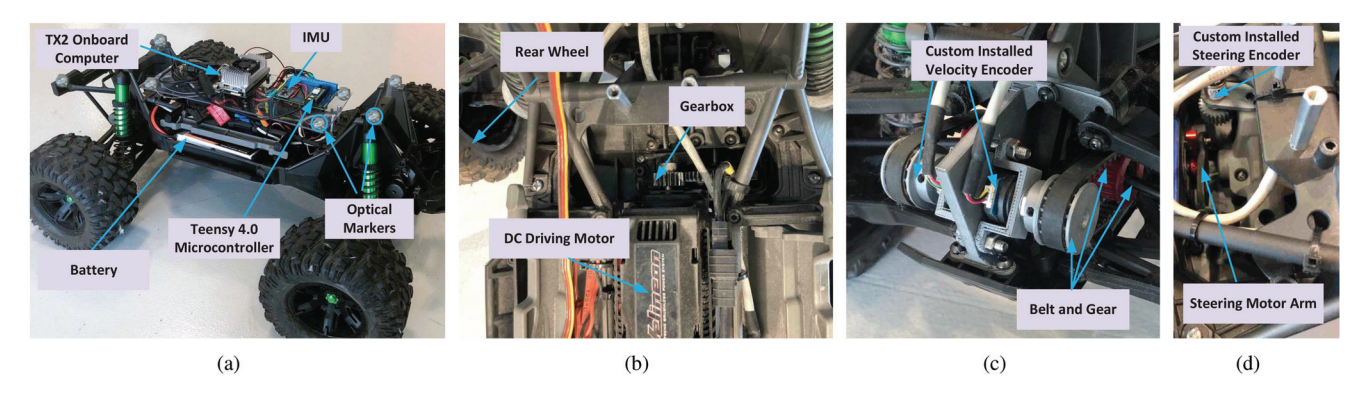


Fig. 3. Modified truck platform. (a) Embedded system on top of a plate. (b) Rear drive motor. (c) Custom-installed velocity encoder. (d) Custom-installed steering encoder.

critical steering angle

$$\phi_c = \tan^{-1} \left(\frac{g l_1 \tan \varphi_G}{v^2} \right). \tag{17}$$

The above relationship implies that a large velocity is required to initiate ski-stunt maneuvers at a reasonable steering angle. From (17), the critical velocity is determined as $v_c = \sqrt{\frac{gl_1 \tan \varphi_G}{\tan \phi_{\max}}}$ by assuming that the maximum allowable steering angle ϕ_{\max} is reached. Once the vehicle body is tilted, the required steering-induced torque is reduced.

1) Stage 2: In this stage, the rolling motion has been initiated and the vehicle enters a transition phase. The vehicle makes a sharp turn with a large steering angle and a roll angle profile φ_e is given by the BEM calculation. The primary concern is rollover prevention. Therefore, we use a similar design as (13) with a simplified object function and constraint as

$$\min_{\boldsymbol{u}_H} \int_t^{t+H\Delta t} e_\varphi^2 d\tau$$
 subj. to : $\dot{\boldsymbol{x}}_s = \boldsymbol{F} + \boldsymbol{G}\boldsymbol{u}_s, \ h_\varphi(\boldsymbol{x}_s) > 0$ (18)

where $h_{\varphi}(x_s) > 0$ denotes the rollover prevention-related CBF in (13d). The solution to (18) is obtained to generate the safe reference profile for x_s and control input u_f is still applied by using x_s .

1) Stage 3: Once the roll angle error is less than a small threshold value, i.e., $|e_{\varphi}| \leq \epsilon$, we recognize that the vehicle has finished the transition phase and is moving to the ski-stunt maneuver. With safety guaranteed, the primary concern becomes trajectory-tracking accuracy. The rollover constraint is still applied and (13) is directly used for motion planning. The controller design in Section III-B is used in this stage.

The above three-stage process deals with initiation and transition from four-wheel operating condition to ski-stunt maneuver. To move back to four-wheel driving mode, the vehicle velocity is reduced to a small value $v_2 < v_c$ and a small (opposite direction) steering angle $\phi_2 < \phi_{\rm max}$ is maintained for a short period of time. The nominal control (10) is used. The entire maneuver switching and control strategy is illustrated and summarized in Fig. 2. The switching conditions from Stages 1 to 2 and 2 to 3 are specified by vehicle velocity $v>v_c$ and roll-angle error $|e_{\varphi}| \leq \epsilon$, respectively. Once in Stage 3, the MPC-CBF

TABLE I
VALUES FOR THE MODEL PARAMETERS OF THE SCALED TRUCK

| m (kg) | $J_t (\mathrm{kgm}^2)$ | l ₁ (m) | l ₂ (m) | y_G (m) | z_G (m) | φ _G (°) |
|--------|-------------------------|--------------------|--------------------|-----------|-----------|--------------------|
| 11.4 | 1.35 | 0.48 | 0.54 | 0.27 | 0.29 | 40 |

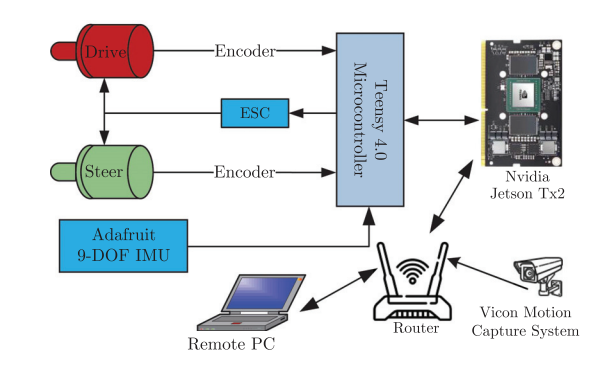


Fig. 4. Schematic of the interconnection of the onboard vehicle mechatronic systems in experiments.

based motion planner computes the safe trajectory r_s , and then balance-enforced control is then used to follow r_d as shown in Algorithm 1.

V. EXPERIMENTAL RESULTS

A. Test Vehicle and Experimental Setup

As shown in Fig. 3(a), the scaled vehicle was built by modifying a radio controlled (RC) truck platform (https://traxxas.com/products/landing/x-maxx/model X-Maxx racing truck from Traxxas). Table I lists the values of the main physical model parameters for the vehicle. The platform is a front-steering, rear-driving scaled truck; see Fig. 3(b). Four encoders and one potentiometer (from US Digital) were installed to measure the front- and rear-wheel angular velocities and the steering angle, respectively; see Fig. 3(c) and (d). The encoders (1024 pulses per each round) were connected to wheel shaft through 3-D printed gears and belts (gear ratio 1:1). One inertia measurement unit (model BNO055 from Adafruit, 9-DOF absolute orientation IMU) was installed to measure the vehicle's roll and yaw angles. The IMU measurement was tested and used for

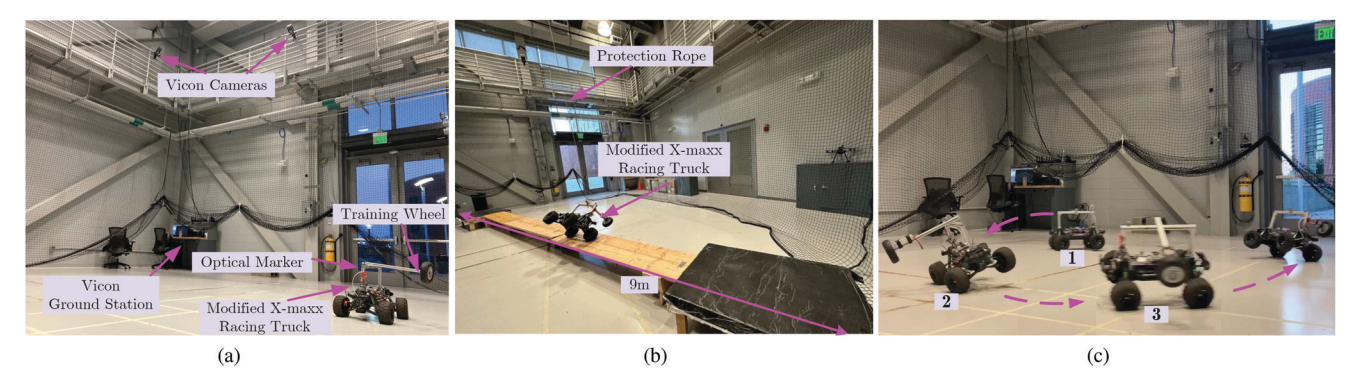


Fig. 5. (a) Indoor experiment setup. (b) Vehicle runs on a narrow bridge by performing a ski-stunt maneuver. (c) Snapshots of ski-stunt maneuver initiation process by steering. The labels in (c) illustrate the stages in four-wheel to two-wheel transition process.

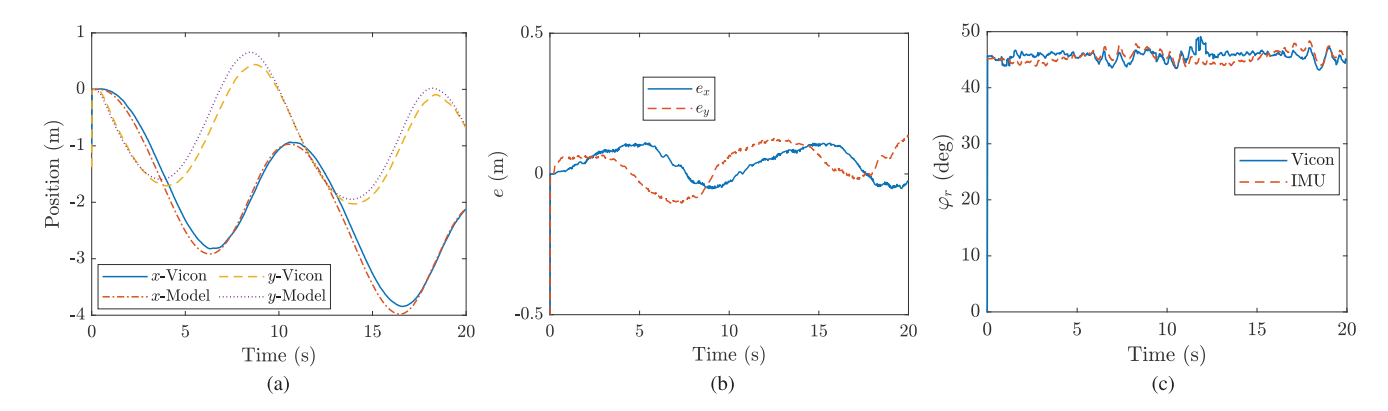


Fig. 6. Onboard sensor-based localization comparison results with the ground truth. (a) Vehicle x and y trajectory comparison. (b) Localization errors. (c) Vehicle roll angle comparison. The initial position and yaw angle were set as zero for sensor-based localization design in experiments.

outdoor tests only. A Jetson TX2 computer (from NVIDIA Inc.) and Teensy 4.0 microcontroller were used for onboard computational sources and also for real-time motion control. The IMU, microcontroller, and TX2 computer were mounted on a flat plate on top of the vehicle.

Fig. 4 shows the schematic of the onboard electronic, actuators, embedded systems, and the rest of the experimental setup. We set up a high-speed wireless local network (5 GHz) and a remote laptop computer was used to communicate with the onboard computing devices. As shown in Fig. 1(a), a training wheel was added and mounted on one side to protect the vehicle from any damage by possible rollover incidents. When the training wheel touched down on the ground, it was found that $\varphi = 8^{\circ}$ and equivalently $\varphi_r = 48^{\circ}$.

The sensor data collection and motion control were implemented in the Robot Operating System with a frequency of 100 Hz (i.e., $\Delta t = 10$ ms). The MPC prediction horizon was set as H = 10. The values of the other control parameters used in experiments are: $\mathbf{W}_1 = \mathrm{diag}(1,1,1,1,10,10), \mathbf{W}_2 = \mathrm{diag}(10,10), \ \gamma_r = [3\ 3\ 20\ 20]^T, \ \gamma_\varphi = [5.5\ 30.5]^T, \ k_{p1} = 6, k_{d1} = 12.5, \ k_{p2} = 14.5, \ k_{d2} = 38, \ \phi_{\mathrm{max}} = 15^\circ, \ \phi_2 = -10^\circ,$ and $v_c = 2.5$ m/s. Given the control input $\mathbf{u}_f = [u_{sv}\ u_{\varphi\psi}]^T,$ the velocity was updated by u_{sv} and the steering angle was calculated as $\phi = \tan^{-1}(\frac{u_{\varphi\psi}l_1\cos\varphi_r}{v})$. The steering angle and

velocity commands were sent to the microcontroller for low-level proportional-integral controller implementation.

We ran experiments primarily in the indoor setup. Limited outdoor experiments were also conducted due to the constrained indoor space for certain runs. Fig. 5(a) shows the indoor experimental setup. The vehicle ran within a 5×5 m² space and a motion capture system (9 Vantage cameras from Vicon Ltd.) was used to provide the vehicle's position and orientation in real time. Optical markers were attached to the vehicle; see Fig. 3(a). For long-distance motion, the experiments were conducted outdoors and the onboard sensing suite (e.g., encoders and IMU) was used to provide localization and orientation of the vehicle since no global positioning system was installed on the vehicle. To validate the performance of the onboard sensorbased localization scheme, we conducted indoor experiments to compare the position and orientation estimation from the onboard sensors with the ground truth from the motion-capture system. Fig. 6 shows the comparison results. Fig. 6(a) shows the vehicle position estimation comparison and Fig. 6(c) for the roll-angle comparison results. The position estimation errors are less than 0.1 m as shown in Fig. 6(b) and the rollangle-estimation error is also small. Therefore, onboard sensorbased localization measurements are accurate for outdoor experiments.

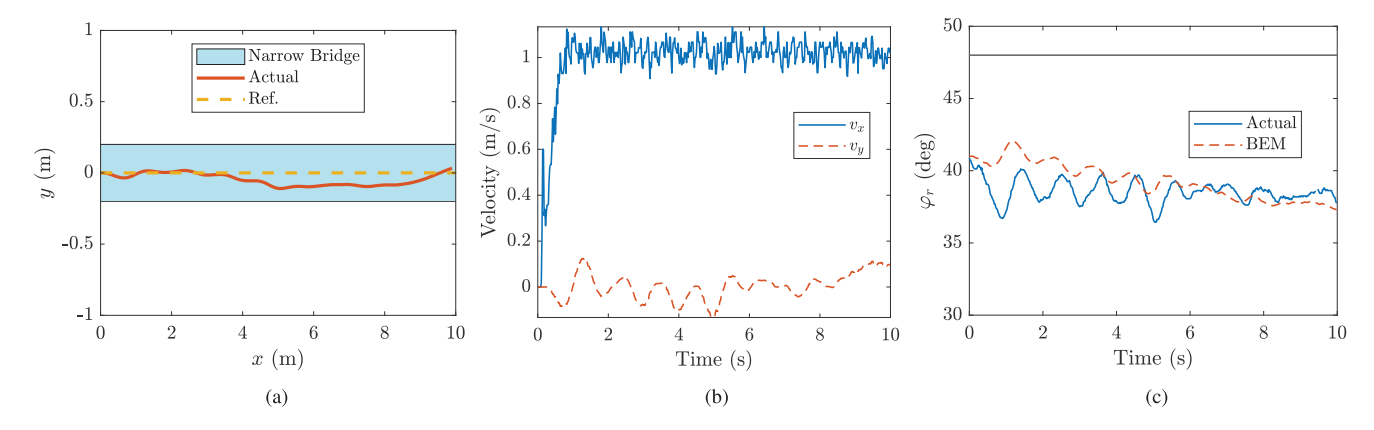


Fig. 7. Experimental results for performing a ski-stunt maneuver to follow a straight-line trajectory on a narrow bridge. (a) Vehicle trajectory. (b) Vehicle longitudinal and lateral velocities. (c) Vehicle roll angle. We added the bias φ_G to the BEM in (c) as the roll angle is in the form of φ_r . The black horizontal line indicates the roll angle $\varphi_r = 48^\circ$ when the training wheel touched the ground.

B. Experimental Results

We first present the results when the roll angle was initially in the neighborhood of the equilibrium point. The purpose is to validate the system model and the results of simultaneous trajectory tracking and safe roll balance. To compare the control performance, the vehicle reference velocity was set at a constant value. Fig. 7 shows the results of the vehicle moving on a narrow wooden deck; see Fig. 5(b) for the experimental setup. The width of the bridge deck was 0.4 m, which was less than the vehicle width ($l_2 = 0.54$ m). The vehicle performed the ski-stunt maneuver to go through the bridge deck in a two-wheeled straight-line trajectory $x_d = 1.2 t$ and $y_d = 0$. Fig. 7(a)-(c) show the vehicle trajectory, velocity, and roll angle profiles, respectively. The trajectory tracking error was within around 0.15 m and the vehicle roll angle followed the equilibrium manifold value closely. One main reason for the position error was due to vibrational disturbances brought on by the flexible training wheel structure installed on the robotic vehicle.

Fig. 8(a)–(c) and (d)–(f) show the trajectory tracking results for straight-line and circular trajectories, respectively. At different moving velocities, the trajectory errors were less than 0.2 m for both types of trajectory profiles. The roll angle displayed small oscillations around the static equilibrium (i.e., $\varphi_{er} = \varphi_e + \varphi_G = 40^\circ$). One benefit of maintaining a fast-moving velocity is that the steering-induced balance torque is large. As shown in Fig. 8(d), the vehicle cannot maintain balance at low velocity (i.e., v = 0.8 m/s). Compared with the straight-line motion, tracking a circular trajectory required a larger balance torque. With a small radius and large velocity, the roll angle becomes small, i.e., farther away from the static equilibrium; see Fig. 8(e). A similar observation can be found when one is riding a bicycle and takes a sharp turn at high speed.

We further show the results for collision avoidance and rollover prevention with the CBF-based constraint-enforced control. Fig. 9(a) shows the vehicle trajectories under ski-stunt maneuver with an obstacle. In the experiment, the obstacle had a circular shape with a radius $R=1\,$ m and its center

at $(x_o, y_o) = (5,0)$ m. The vehicle should avoid the obstacle and perform a ski-stunt maneuver when moving from the origin to the target position at (10, 0) m. We used the CBF $h_r(x)$ in (12). It is not a surprise that in Fig. 9(d) the vehicle would hit the obstacle when the CBF-related constraint was not used. With the CBF constraint enforced, the vehicle passed the obstacle and maintained its balance. Fig. 9(b) and (c) shows the vehicle roll angle φ_r and its error during the maneuver. It is interesting to note that with a large velocity, the safe distance from the vehicle to the obstacle became larger, as shown in Fig. 9(d). A fast velocity implies an aggressive, high-risk motion and therefore, the conservative control was taken by the design.

Fig. 10 shows the ski-stunt maneuver initiation results. The trajectory tracking task was not enforced in this experiment. The vehicle speed was set as 2.5 m/s. At t = 2 s, a sharp turn was taken to initiate the ski-stunt maneuver. The CBF was constructed with $\varphi_1=22$ and $\varphi_2=20^\circ$ and therefore, the maximum allowed roll angle was set at $\varphi_{\rm max}=42^{\circ}$. The targeted roll angles were commanded at $\varphi_r^c=20^\circ$ and 30° ($\varphi=-20^\circ$ and -10° , equivalently). As shown in Fig. 10(a) and (c), the vehicle safely tilted its body without exceeding the boundary and the roll angle errors were within 5°. In contrast, rollover happened (rotation angle is beyond $\varphi_r = 48^\circ$) when the CBF constraint was not applied. To prevent rollover, the roll angle dropped back to 10° at t = 4.5 s immediately when reaching 40° , shown in Fig. 10(a). The $\varphi_r^c = 20^\circ$ reference was farther away from the static equilibrium and thus, required a large balance torque. The steering angle for $\varphi_r^c = 20^\circ$ was larger than that of $\varphi_r^c = 30^\circ$, as shown in Fig. 10(b). Fig. 5(c) shows a snapshot of one initiation experiment run.

We next demonstrate the autonomous ski-stunt maneuver and motion-switching results. Fig. 11(a) shows the vehicle trajectory during the experiment. The vehicle started from the origin and followed a circular trajectory with a radius of $1.2 \, \mathrm{m}$ in four-wheel driving mode. It started at Stage 1 of the ski-stunt maneuver initiation process and accelerated to velocity $v=2.5 \, \mathrm{m/s}$ at $t=1.5 \, \mathrm{s}$. Then, the initiation process transitioned to Stage 2 with

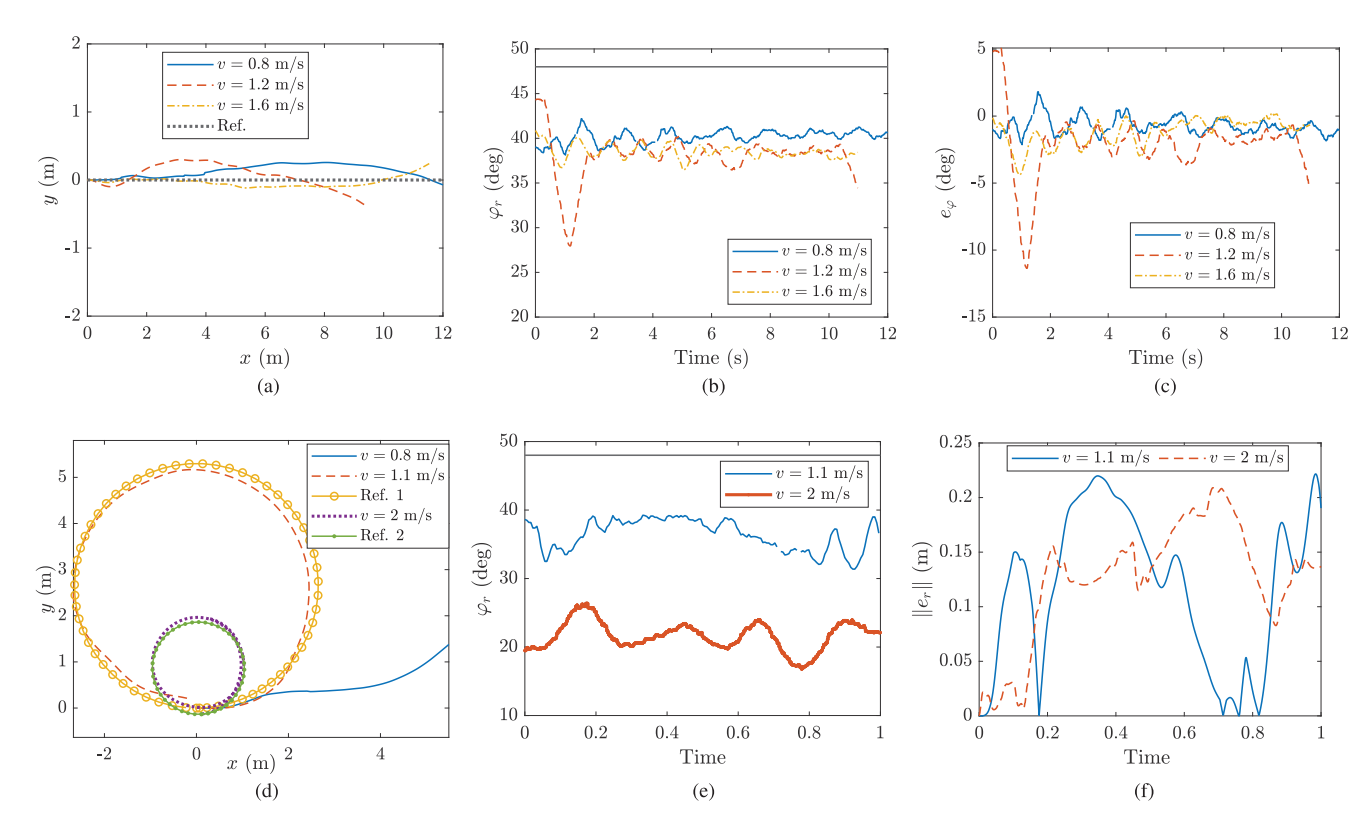


Fig. 8. Comparison results of ski-stunt maneuvers for following a straight-line (outdoor experiments) and circular trajectories with different velocities. Vehicle trajectory, roll angle, and roll angle error: (a)–(c) for straight-line trajectory; (d)–(f) for circular trajectory. The black horizontal lines in (b) and (e) indicate the roll angle $\varphi_r = 48^\circ$ when the training wheel touched the ground.

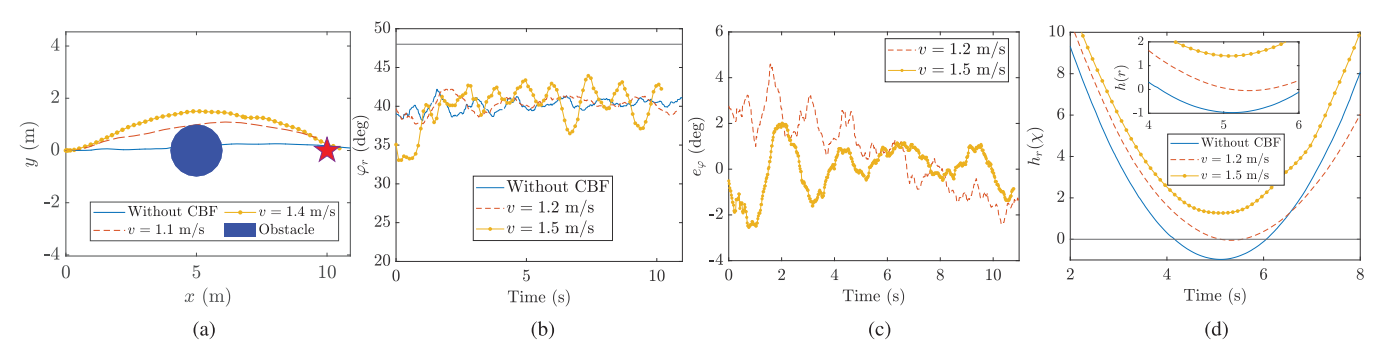


Fig. 9. Outdoor experiments for obstacle avoidance in ski-stunt maneuver. (a) Vehicle trajectory. (b) Vehicle roll angle. The black horizontal line indicates the roll angle $\varphi_r = 48^\circ$ when the training wheel touched the ground. (c) Roll angle error. (d) CBF function $h_r(x)$.

steering angle $\phi_{\rm max}=15^\circ$. The calculated BEM $\varphi_e=-18^\circ$ was used as the reference roll angle. We selected the rollover prevention CBF with $\varphi_1=22^\circ$ and $\varphi_2=20^\circ$. The vehicle smoothly entered the ski-stunt motion without large rolling oscillation. Starting from t=3 s, the vehicle performed the ski-stunt maneuver (i.e., Stage 3) and the roll angle followed the desired angle with trajectory tracking error around 0.3 m, as shown in Fig. 11(b). At t=10 s, the vehicle velocity reduced to v=1.5 m/s (Fig. 11(c)) and a steering angle was commanded to exit the ski-stunt maneuver and move back to four-wheel driving to follow a large circular trajectory with a radius of 1.5 m (for 10 s).

The vehicle initiated the second ski-stunt maneuver at $t=20\,\mathrm{s}$ to follow an elliptical trajectory (long and short semiaxes of 2.25 m and 1.5 m, respectively). The calculated BEM was around $\varphi_e=-5^\circ$ (i.e., $\varphi_{er}=35^\circ$; see Fig. 11(d)). The vehicle velocity increased to around $v=2.9\,\mathrm{m/s}$ to take the sharp turn. The steering angle was first set to the right direction (i.e., around $\phi=-10^\circ$) for a short time and then turned back to around $\phi=8^\circ$ to start Stage 1 of the ski-stunt maneuver initiation process. As shown in Fig. 11(e), this stage lasted for about 3 s, and then moved to Stage 2 for another 2 s to enter the steady ski-stunt maneuver. The vehicle followed the BEM $\varphi_{er}=35^\circ$ along the elliptical trajectory. The

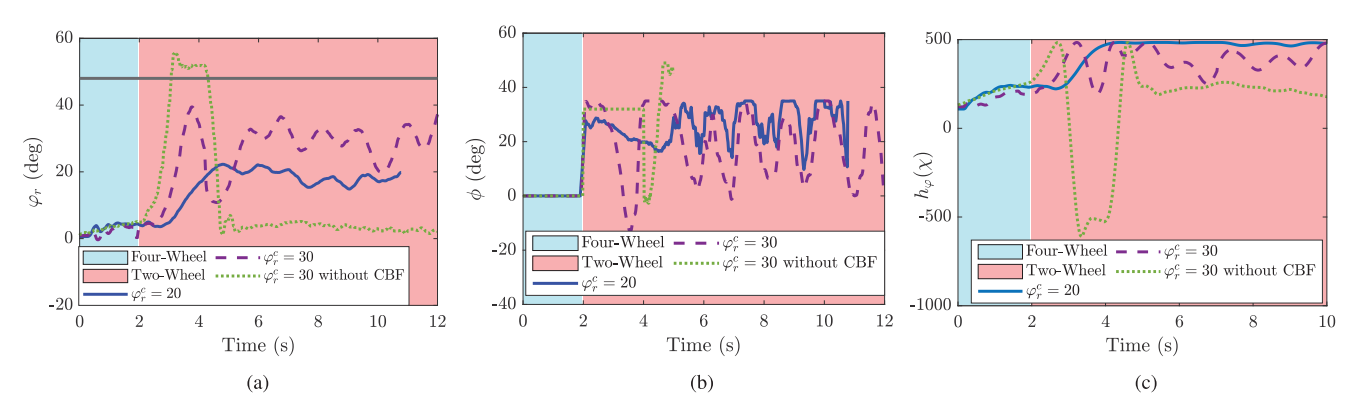


Fig. 10. Experimental results for ski-stunt maneuver initiation with various control designs. (a) Vehicle roll angle. The black horizontal line indicates the roll angle $\varphi_r = 48^\circ$ when the training wheel touched the ground. (b) Vehicle steering angle. (c) CBF function value $h_{\varphi}(x)$. The light blue and pink colors indicate the four- and two-wheel driving modes, respectively.

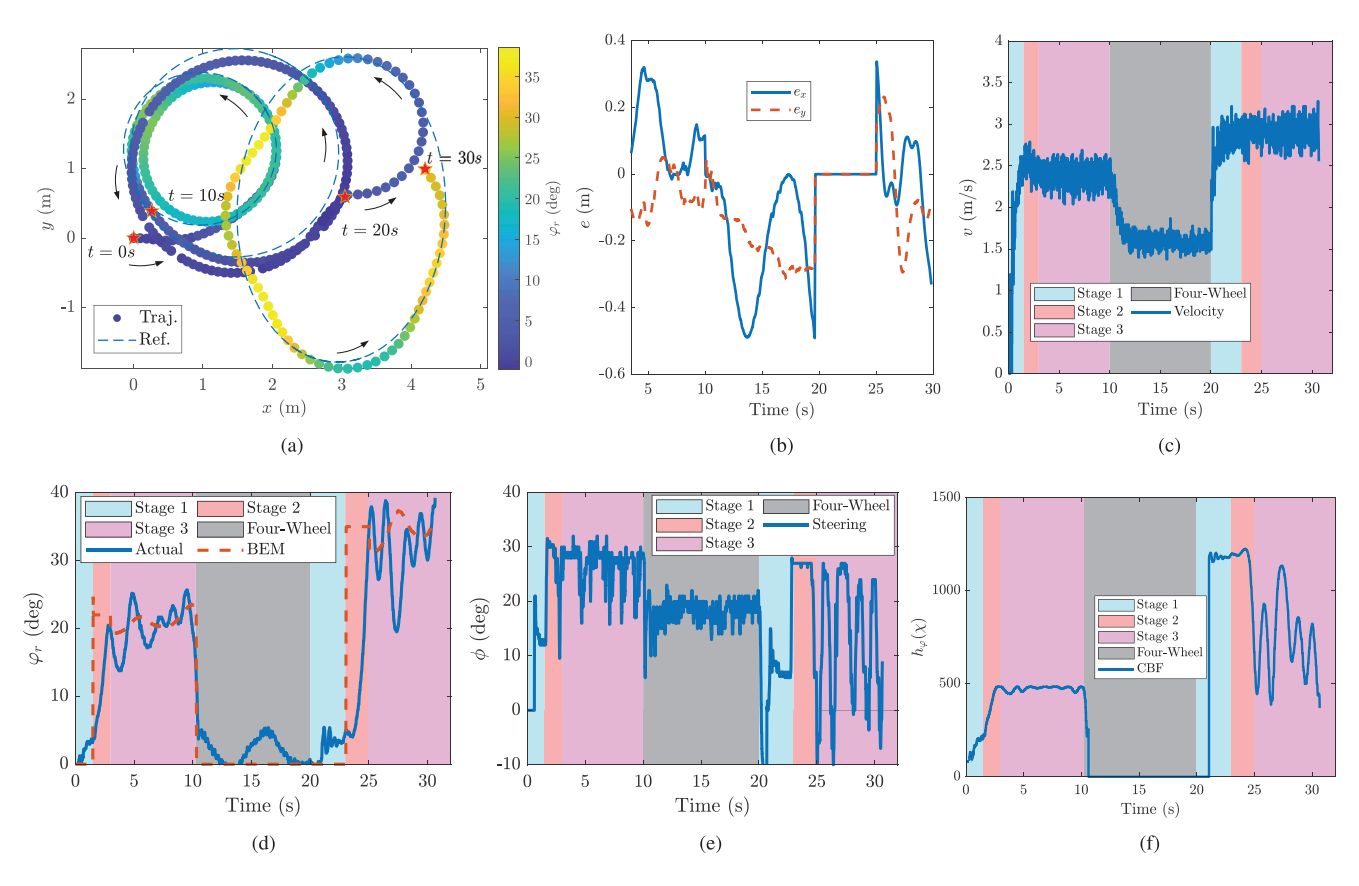


Fig. 11. Experimental demonstration of switching strategies between regular four-wheel driving and a ski-stunt maneuver. (a) Vehicle actual and reference trajectories. (b) Trajectory tracking error. (c) Vehicle velocity magnitude. (d) Roll angle φ . (e) Steering angle ϕ . (f) Rollover prevention CBF $h_{\varphi}(x)$. The colors in (c)–(f) indicate the different stages of the ski-stunt maneuver initiation process.

CBF was designed with $\varphi_1=35^\circ$ and $\varphi_2=30^\circ$. Fig. 11(f) shows the CBF values during the entire experimental run. It is clear to see that the roll angle followed the targeted profiles without overshooting and the CBF also confirmed the safety of the vehicle maneuver. The results verified that under the proposed control algorithm, the vehicle performed safe ski-stunt maneuvers.

C. Discussion

In experiments, the roll angles showed some oscillations. This was partially due to the effect of the flexible suspension design of the RC truck. The installed training wheel structure also caused additional roll-motion oscillation when the vehicle was performing ski-stunt maneuvers. To initiate the ski-stunt motion,

it is preferable for a vehicle to have a high CoM. However, a high CoM requires a large balance torque to maintain balance. This tradeoff feature adds difficulty in designing the motion controller for ski-stunt maneuvers. Starting from four-wheel driving conditions, a sharp turn is required to generate significant steering-induced torque to initiate and keep tilting the vehicle body, while rollover prevention is necessary. For most human-performed ski-stunt maneuvers, a ramp is used to first tilt the vehicle body so that the steering angle can be kept at around zero. In our work, we did not use any ramps to help initiate ski-stunt maneuvers. To avoid the large change of the steering angle after the maneuver initialization, the BEM was used for the roll-balance profile. Meanwhile, the vehicle velocity was selected by using the calculation in (17). These considerations enhanced the control performance.

In this work, the planar motion of the scaled vehicle was built on the kinematics model (with the nonholonomic constraint), while the roll motion was based on a dynamics model. The tire–road friction in the experiment setup was high and the kinematic model was accurate enough to capture the vehicle's planar motion. We can additionally consider dynamics model for the vehicle motion, along with the tire–road interactions that are important for planning of aggressive motions. However, obtaining the friction model parameters would add further complexity to the systems modeling and control design. Furthermore, the model and control parameters have to be tuned to physical system variations wear of the tires, among other factors [24], [25].

We can use tire–road interaction models to analyze the effect of large tire-slip and camber angles in ski-stunt maneuver on tire friction forces. The front-tire slip angle is given as $\alpha_f = \tan^{-1}(l_1\dot{\psi}/v) - \phi$ and the lateral force of the front tire at fourwheel driving condition is calculated as [26]

$$F_y = D_y \sin \left(C_y \tan^{-1} \left(B_y \alpha_f \right) \right) \tag{19}$$

where D_y , C_y , and B_y are the model parameters. When initiating a ski-stunt maneuver, a sharp turn was used to increase α_f , and therefore lateral force F_y . A large force F_y created significant turning torques to tilt the vehicle body. Fig. 12 shows the α_f profile for the experiment run with $\varphi_r^c = 20^\circ$ (Fig. 10). Clearly, a large slip angle (in magnitude) occurred at t=2 s when the ski-stunt initiation started. Once the vehicle body was tilted, the support tire experienced a large camber angle φ_r and the lateral force is then modeled as [27]

$$F_{y} = \frac{D_{y}}{1 + a_{1}\varphi_{x}^{2}} \sin\left(C_{y} \tan^{-1} \frac{B_{y}\alpha_{f}}{1 + a_{2}\varphi_{x}^{2}}\right)$$

where $a_1, a_2 \ge 0$ are tire model parameters. Compared to (19), with the same slip angle α_f , the lateral force F_y is significantly reduced under large camber angle (i.e., φ_r). This implies that steering actuation becomes much less effective during ski-stunt maneuvers than that in regular four-wheel driving condition.

We can further improve ski-stunt maneuver performance in several aspects. The use of training wheels in experiments brought oscillations in roll angles and position errors and we should improve the design to increase the structural rigidity of the vehicle system. Due to the large tilt angle, wear and tear

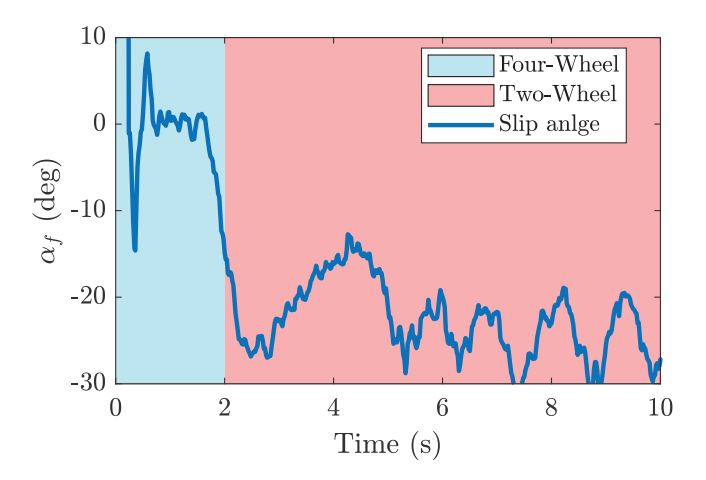


Fig. 12. Front wheel slip angle in ski-stunt initiation experiment with $\varphi_r=20^\circ.$

significantly damaged the tires and changed the tire-road interaction properties. This also affected the steering actuation effectiveness and the control designs had to adapt to those changes. We only tested the control method on even and flat ground surfaces with high friction coefficient. The control design might need to be revised for high-speed ski-stunt maneuver on rough, off-road terrain. Towards to this goal, dynamics model must be used for the vehicle motion control and tire-road interactions should be incorporated into the motion planning. Moreover, it is desirable to conduct full-size vehicle implementation and testing for autonomous ski-stunt maneuvers. Full-size vehicles display multibody dynamics properties and the motion model used in the article might no longer apply. System identification and machine learning-based methods can be further considered [26], [28], [29]. This work mainly focuses on the motion-control task and motion planning for the ski-stunt maneuver is not fully explored. To achieve higher-performance autonomous maneuvers, an effective motion planner still needs to be developed and integrated with the motion control [30].

VI. CONCLUSION

This article has presented a motion-control design for autonomous vehicle ski-stunt maneuvers. The vehicle motion under ski-stunt maneuvers shares similar dynamic behavior with rollovers, but the rolling motion was stabilized around an (unknown) dynamic equilibrium. We designed the CBF-based dynamic constraint for online safe roll-trajectory planning and incorporated it into an MPC approach. The external and internal convertible form-based control was used for trajectory tracking with safety-guaranteed roll motion. We further presented a motion-switching strategy between the autonomous ski-stunt maneuver and regular four-wheel driving control. Under the proposed design, the ski-stunt maneuver was proved to be stable and safe. The motion control strategies were validated and demonstrated extensively through experiments on a scaled vehicle platform. As a future research direction, the model accuracy should be improved to enhance the performance. Development of machine learning-based motion control is another ongoing research direction for both the motion-planning and control tasks.

APPENDIX

We first show that under control u_f , error $e_x = [e_s^T \ e_{\varphi} \ \dot{e}_s^T \ \dot{e}_{\varphi}]^T$ converges a small ball around the origin exponentially. From (15), we obtain $u_{s\psi} = -g_{\varphi}^{-1} f_{\varphi}$ under the condition $\varphi = \varphi_e$. We rewrite the updated control $u_{\varphi\psi}$ around $\varphi = \varphi_e$, $\dot{\varphi} = \ddot{\varphi} = 0$ as

$$u_{\varphi\psi} = g_{\varphi}^{-1} \left(-f_{\varphi} + \ddot{\varphi}_{e} - k_{p2}e_{\varphi} - k_{d2}\dot{e}_{\varphi} \right)$$

$$= u_{s\psi} + \mathcal{O}(e_{\varphi}) + g_{\varphi}^{-1} \left(\ddot{\varphi}_{e} - k_{p2}e_{\varphi} - k_{d2}\dot{e}_{\varphi} \right)$$

$$= u_{s\psi} + \mathcal{O}(e_{\varphi}) + g_{\varphi}^{-1}v_{\varphi}$$
(20)

where $\mathcal{O}(e_{\varphi})$ denotes the higher order terms. Under control u_f , the error dynamics with respect to the safe trajectory r_s is obtained by using (20)

$$\ddot{e}_s = -k_{p1}e_s - k_{d1}\dot{e}_s + p_r, \ \ddot{e}_{\varphi} = -k_{p2}e_{\varphi} - k_{d2}\dot{e}_{\varphi} + p_{\varphi}$$
(21)

where $p_r = g_r(v,\psi)[0 \ \mathcal{O}(e_\varphi) + g_\varphi^{-1}v_\varphi]^T$ and p_φ are perturbation terms due to the coupling between the planar and roll motion with the BEM. The closed-loop dynamics (21) is then rewritten as a compact form as

$$\dot{\boldsymbol{e}}_x = \boldsymbol{D}\boldsymbol{e}_x + \boldsymbol{p}$$

where matrix D is composed of the feedback gains k_{p1} , k_{d1} , k_{p2} , and k_{d2} , and perturbation term $\boldsymbol{p} = [\boldsymbol{0}_2^T \ 0 \ \boldsymbol{p}_r^T \ p_\varphi]^T$. We introduce the Lyapunov function $V_1 = \frac{1}{2}\boldsymbol{e}_x^T\boldsymbol{e}_x$. By as-

We introduce the Lyapunov function $V_1 = \frac{1}{2} \boldsymbol{e}_x^T \boldsymbol{e}_x$. By assumption of the perturbation term is affine of error \boldsymbol{e}_x , there exists $c_1, c_2 > 0$ such that $\|\boldsymbol{p}\| \le c_1 \|\boldsymbol{e}_x\| + c_2$. Under this condition, we obtain

$$\dot{V}_{1} = \boldsymbol{e}_{x}^{T} \left(\boldsymbol{D} \boldsymbol{e}_{x} + \boldsymbol{p} \right) \leq \boldsymbol{e}_{x}^{T} \boldsymbol{D} \boldsymbol{e}_{x} + \|\boldsymbol{e}_{x}\| \left(c_{1} \|\boldsymbol{e}_{x}\| + c_{2} \right)
\leq \left[\lambda_{\max}(\boldsymbol{D}) + c_{1} \right] \|\boldsymbol{e}_{x}\|^{2} + c_{2} \|\boldsymbol{e}_{x}\|.$$

Let the control gains be properly selected such that $\lambda_{\max}(D) + c_1 < 0$, where $\lambda_{\max}(D)$ is the greatest eigenvalue of D. Thus, the error e_x converges to zero until enters a small ball.

We denote the safe control input after the CBF filtering as $u_s^* = u_n + e_u^*$, where e_u^* is the CBF modification to the nominal control. The planning error becomes

$$\ddot{e}_{1} = \ddot{r}_{s} - \ddot{r}_{d} = g_{r}^{-1}(u_{n} + e_{u}^{*}) - \ddot{r}_{d}$$

$$= -k_{d1}\dot{e}_{r} - k_{p1}e_{r} + g_{r}^{-1}e_{u}^{*}$$

$$= -k_{d1}(\dot{e}_{1} + \dot{e}_{s}) - k_{p1}(e_{1} + e_{s}) + g_{r}^{-1}e_{u}^{*}.$$
(22)

Combining with the e_s dynamics in (21), we have planar motion error relative the reference is $e_r = r - r_d = (r - r_s) + (r_s - r_d) = e_s + e_1$, where $e_1 = r_s - r_d$, and its dynamics is calculated as

$$\ddot{e}_r = -k_{d1}(\dot{e}_s + \dot{e}_1) - k_{n1}(e_s + e_1) + p_r + q_r^{-1}e_n^*$$

Note that the total control error $e_r = e_s + e_1$ consists of control error e_s and the planning error e_1 is captured by (22). The convergence of error has been shown above and now we need to prove the convergence of error e_1 .

Since V_1 converges to a ball near zero exponentially regardless of the error e_1 , we assume that after finite time under the control u_f , e_s is small enough, i.e., $\|[e_s^T\ \dot{e}_s^T]^T\| \le \epsilon_s$ with $\epsilon_s > 0$. The e_1 dynamics then becomes $\dot{e}_1 = -k_{d1}\dot{e}_1 - k_{p1}e_1 + p_s$, where $p_s = p_r + g_r^{-1}e_u^* + ([k_{p1}\ k_{d1}]^T\epsilon_s)$. The convergence of e_1 can be shown by taking the Lyapunov function candidate $V_2 = \frac{1}{2}e_d^Te_d$, where $e_d = [e_1^T\ \dot{e}_1^T]^T$. The time derivative of V_2 is

$$egin{aligned} \dot{V}_2 &= oldsymbol{e}_d^T egin{bmatrix} oldsymbol{0}_{2 imes 2} & oldsymbol{I}_2 \ -k_{p1}oldsymbol{I}_2 & -k_{d1}oldsymbol{I}_2 \end{bmatrix} oldsymbol{e}_d + \dot{oldsymbol{e}}_1^T oldsymbol{p}_s \ &\leq -oldsymbol{e}_d^T oldsymbol{\Lambda} oldsymbol{e}_d + \|oldsymbol{e}_d\|\|oldsymbol{p}_s\|. \end{aligned}$$

With $k_{p1}, k_{d1} > 0$, Λ is negative definite. Since $||p_s||$ is bounded, e_1 converges to a small ball around zero. Therefore, under u_f , the trajectory r converges to a neighborhood of r_d and $x \in \mathcal{S}$, and $\varphi \in \mathcal{E}$ are achieved. This completes the proof.

REFERENCES

- J. Yi, J. Li, J. Lu, and Z. Liu, "On the dynamic stability and agility of aggressive vehicle maneuvers: A pendulum-turn maneuver example," *IEEE Trans. Contr. Syst. Technol.*, vol. 20, no. 3, pp. 663–676, May 2012.
- [2] J. Y. Goh, T. Goel, and J. C. Gerdes, "Toward automated vehicle control beyond the stability limits: Drifting along a general path," ASME J. Dyn. Syst., Meas., Control, vol. 142, no. 1, 2020, Art. no. 021004.
- [3] A. Arab, K. Yu, J. Yu, and J. Yi, "Motion planning and control of autonomous aggressive vehicle maneuvers," *IEEE Trans. Automat. Sci. Eng.*, to be published, doi: 10.1109/TASE.2023.3245948.
- [4] B. Springfeldt, "Rollover of tractors International experiences," Saf. Sci., vol. 24, no. 2, pp. 95–110, 1996.
- [5] H. Imine, L. M. Fridman, and T. Madani, "Steering control for rollover avoidance of heavy vehicles," *IEEE Trans. Veh. Technol.*, vol. 61, no. 8, pp. 3499–3509, Oct. 2012.
- [6] R. Eger and U. Kiencke, "Modeling of rollover sequences," IFAC Proc. Volumes, vol. 33, no. 26, pp. 121–126, 2000.
- [7] G. Phanomchoeng and R. Rajamani, "Real-time estimation of rollover index for tripped rollovers with a novel unknown input nonlinear observer," *IEEE/ASME Trans. Mechatronics*, vol. 19, no. 2, pp. 743–754, Apr. 2014.
- [8] G. Phanomchoeng and R. Rajamani, "New rollover index for the detection of tripped and untripped rollovers," *IEEE Trans. Ind. Electron.*, vol. 60, no. 10, pp. 4726–4736, Oct. 2013.
- [9] J. Lu, D. Messih, and A. Salib, "Roll rate based stability control The roll stability control system," in *Proc. 20th Int. Tech. Conf. Enhanced Saf.* Veh., 2007, Art. no. 07-0136.
- [10] N. Getz, "Dynamic inversion of nonlinear maps with applications to nonlinear control and robotics," Ph.D. dissertation, Dept. Electr. Eng. and Comp. Sci., Univ. California, Berkeley, CA, USA, 1995.
- [11] V. Cossalter, Motorcycle Dynamics. Greendale, WI, USA: Race Dynamics, 2002.
- [12] J. Yi, D. Song, A. Levandowski, and S. Jayasuriya, "Trajectory tracking and balance stabilization control of autonomous motorcycles," in *Proc. IEEE Int. Conf. Robot. Autom.*, 2006, pp. 2583–2589.
- [13] P. Wang, J. Yi, T. Liu, and Y. Zhang, "Trajectory tracking and balance control of an autonomous bikebot," in *Proc. IEEE Int. Conf. Robot. Autom.*, Singapore, 2017, pp. 2414–2419.
- [14] P. Wang, J. Yi, and T. Liu, "Stability and control of a rider-bicycle system: Analysis and experiments," *IEEE Trans. Automat. Sci. Eng.*, vol. 17, no. 1, pp. 348–360, Jan. 2020.
- [15] A. D. Ames, S. Coogan, M. Egerstedt, G. Notomista, K. Sreenath, and P. Tabuada, "Control barrier functions: Theory and applications," in *Proc. Europ. Control Conf.*, 2019, pp. 3420–3431.
- [16] M. Khan, T. Ibuki, and A. Chatterjee, "Safety uncertainty in control barrier functions using gaussian processes," in *Proc. IEEE Int. Conf. Robot. Autom.*, 2021, pp. 6003–6009.

- [17] J. Seo, J. Lee, E. Baek, R. Horowitz, and J. Choi, "Safety-critical control with nonaffine control inputs via a relaxed control barrier function for an autonomous vehicle," *IEEE Robot. Automat. Lett.*, vol. 7, no. 2, pp. 1944–1951, Apr. 2022.
- [18] F. Han and J. Yi, "Stable learning-based tracking control of underactuated balance robots," *IEEE Robot. Automat. Lett.*, vol. 6, no. 2, pp. 1543–1550, Apr. 2021.
- [19] F. Han and J. Yi, "Learning-based safe motion control of vehicle ski-stunt maneuvers," in *Proc. IEEE/ASME Int. Conf. Adv. Intelli. Mechatronics*, 2022, pp. 724–729.
- [20] K. Chen, Y. Zhang, J. Yi, and T. Liu, "An integrated physical-learning model of physical human-robot interactions with application to pose estimation in bikebot riding," *Int. J. Robot. Res.*, vol. 35, no. 12, pp. 1459–1476, 2016.
- [21] A. Arab and J. Yi, "Instructed reinforcement learning control of safe autonomous J-turn vehicle maneuvers," in *Proc. IEEE/ASME Int. Conf. Adv. Intelli. Mechatron.*, 2021, pp. 1058–1063.
- [22] Q. Nguyen and K. Sreenath, "Exponential control barrier functions for enforcing high relative-degree safety-critical constraints," in *Proc. IEEE Amer. Control Conf.*, 2016, pp. 322–328.
- [23] A. Taylor, A. Singletary, Y. Yue, and A. Ames, "Learning for safety-critical control with control barrier functions," in *Proc. 2nd Conf. Learn. Dyn. Control*, 2020, pp. 708–717.
- [24] R.-C. Roman et al., "Iterative feedback tuning algorithm for tower crane systems," *Procedia Comput. Sci.*, vol. 199, pp. 157–165, 2022.
- [25] R.-E. Precup and S. Preitl, "Optimisation criteria in development of fuzzy controllers with dynamics," *Eng. Appl. Artif. Intelli.*, vol. 17, no. 6, pp. 661–674, 2004.
- [26] J. Kabzan, L. Hewing, A. Liniger, and M. N. Zeilinger, "Learning-based model predictive control for autonomous racing," *IEEE Robot. Automat. Lett.*, vol. 4, no. 4, pp. 3363–3370, Oct. 2019.
- [27] A. Mansour, T. Chen, K. Amir, and J. Soo, "Active camber system for lateral stability improvement of urban vehicles," *Proc. Inst. Mech. Eng.*, *Part D: J. Automobile Eng.*, vol. 233, no. 14, pp. 3824–3838, 2019.
- [28] M. Mihalec and J. Yi, "Balance gait controller for a bipedal robotic walker with foot slip," *IEEE/ASME Trans. Mechatron.*, vol. 28, no. 4, pp. 2012–2019, Aug. 2023, doi: 10.1109/TMECH.2023.3281463.
- [29] K. Chen, J. Yi, and D. Song, "Gaussian-process-based control of underactuated balance robots with guaranteed performance," *IEEE Trans. Robot.*, vol. 39, no. 1, pp. 572–589, Feb. 2023.
- [30] P. Cai, H. Wang, H. Huang, Y. Liu, and M. Liu, "Vision-based autonomous car racing using deep imitative reinforcement learning," *IEEE Robot. Automat. Lett.*, vol. 6, no. 4, pp. 7262–7269, Oct. 2021.



Feng Han (Graduate Student Member, IEEE) received the B.S. degree in aerospace engineering from the Nanjing University of Aeronautics and Astronautics, Nanjing, China, in 2017, and the M.S. degree in aerospace engineering from the Harbin Institute of Technology, Harbin, China, in 2019. He is currently working toward the Ph.D. degree in mechanical and aerospace engineering with Rutgers University, Piscatawav. NJ. USA.

His research interests include dynamics, control, and machine learning with applications to robotics.



Jingang Yi (Senior Member, IEEE) received the B.S. degree in electrical engineering from Zhejiang University, Hangzhou, China, in 1993, the M.Eng. degree in precision instruments from Tsinghua University, Beijing, China, in 1996, and the M.A. degree in mathematics and the Ph.D. degree in mechanical engineering from the University of California, Berkeley, CA, USA, in 2001 and 2002, respectively.

He is currently a Professor of mechanical engineering with Rutgers University, Piscataway,

NJ, USA. His research interests include autonomous robotic systems, mechatronics, dynamic systems, and controls.

Dr. Yi was a recipient of the 2010 US NSF CAREER Award. He currently serves as a Senior Editor for the *IEEE Robotics and Automation Letters* and IEEE TRANSACTIONS ON AUTOMATION SCIENCE AND ENGINEERING. He is a Fellow of the American Society of Mechanical Engineers (ASME).